

This is a repository copy of *Measurement of magnetic cavitation driven by heat flow in a plasma*.

White Rose Research Online URL for this paper:

<https://eprints.whiterose.ac.uk/200261/>

Version: Accepted Version

---

**Preprint:**

Arran, Christopher [orcid.org/0000-0002-8644-8118](https://orcid.org/0000-0002-8644-8118), Dearling, Adam, Bradford, Philip et al. (13 more authors) (Accepted: 2023) Measurement of magnetic cavitation driven by heat flow in a plasma. [Preprint] (In Press)

---

**Reuse**

This article is distributed under the terms of the Creative Commons Attribution (CC BY) licence. This licence allows you to distribute, remix, tweak, and build upon the work, even commercially, as long as you credit the authors for the original work. More information and the full terms of the licence here:

<https://creativecommons.org/licenses/>

**Takedown**

If you consider content in White Rose Research Online to be in breach of UK law, please notify us by emailing [eprints@whiterose.ac.uk](mailto:eprints@whiterose.ac.uk) including the URL of the record and the reason for the withdrawal request.

# Measurement of magnetic cavitation driven by heat flow in a plasma

C. Arran,<sup>1,\*</sup> P. Bradford,<sup>1,†</sup> A. Dearling,<sup>1</sup> G. S. Hicks,<sup>2</sup> S. Al-Atabi,<sup>2</sup> L. Antonelli,<sup>1</sup>  
O. C. Ettliger,<sup>2</sup> M. Khan,<sup>1</sup> M. P. Read,<sup>1,‡</sup> K. Glize,<sup>3,§</sup> M. Notley,<sup>3</sup> C. A.  
Walsh,<sup>4,¶</sup> R. J. Kingham,<sup>5</sup> Z. Najmudin,<sup>2</sup> C. P. Ridgers,<sup>1</sup> and N. C. Woolsey<sup>1</sup>

<sup>1</sup>*York Plasma Institute, Department of Physics, University of York, YO10 5DD*

<sup>2</sup>*The John Adams Institute for Accelerator Science,*

*Blackett Laboratory, Imperial College London, London SW7 2BZ, UK*

<sup>3</sup>*Central Laser Facility, STFC Rutherford Appleton Laboratory, Oxfordshire OX11 0QX, UK*

<sup>4</sup>*Lawrence Livermore National Laboratory, 7000 East Ave., Livermore, CA 94550-9234*

<sup>5</sup>*Blackett Laboratory, Imperial College London, London SW7 2BZ, UK*

We describe the direct measurement of the expulsion of a magnetic field from a plasma driven by heat flow. Using a laser to heat a column of gas within an applied magnetic field, we isolate Nernst advection and show how it changes the field over a nanosecond timescale. Reconstruction of the magnetic field map from proton radiographs demonstrates that the field is advected by heat flow in advance of the plasma expansion with a velocity  $v_N = (6 \pm 2) \times 10^5$  m/s. Kinetic and extended magnetohydrodynamic simulations agree well in this regime due to the build-up of a magnetic transport barrier.

In extreme pressures and temperature gradients, heat flow and magnetic fields are strongly coupled, but although theoretical work shows that strong heat flows can cause significant changes in the magnetic field [1–3], it has long proven difficult to measure these changes experimentally. A particular challenge in magnetised plasma experiments is Nernst-driven magnetic cavitation, in which heat flow causes expulsion of the magnetic field from the hottest regions of a plasma. This reduces the effectiveness of magnetised fusion techniques [4, 5], where strong magnetic fields are employed to confine the heat inside the plasma and increase yield [6–9].

The Nernst effect is familiar in semiconductors and has been measured in semi-metals and even superconductors [10]. In all of these cases, mobile charge carriers in a temperature gradient are deflected by a perpendicular magnetic field. The larger gyroradii and lower collision frequency of particles at higher temperatures results in net momentum of carriers perpendicular to both the temperature gradient and the magnetic field, establishing an electric field. In plasmas, this is typically described using classical transport theory by the thermal force acting on electrons as  $\mathbf{F}_\perp \propto -\nabla T_e \times \mathbf{B}$  [2]. When the Nernst electric field has a non-zero curl, the net motion of charge carriers drives advection of the magnetic field as  $\partial \mathbf{B} / \partial t = \nabla \times (\mathbf{v}_N \times \mathbf{B})$ , where the Nernst advection velocity is given by  $\mathbf{v}_N \approx 2\phi_q / 5n_e T_e$  for a heat flow  $\phi_q$  [3, 11]. That is, the magnetic field is transported down temperature gradients by heat flow as well as being transported down pressure gradients by bulk plasma flow. This Nernst advection causes expulsion of the magnetic field from a hot plasma without a corresponding change in the plasma density profile, a result which cannot be explained by common models using purely ideal or resistive magnetohydrodynamics (MHD).

In general, Nernst advection is the dominant means of magnetic field transport wherever the speed of the heat

flow is faster than both the bulk motion and the rate of magnetic dissipation; previous experiments which measured the Biermann battery in laser-solid interactions have shown that models of magnetised plasmas which neglect the Nernst effect fail during fast heating processes [12–16]. Furthermore, because heat flow depends on higher order moments of the velocity distribution, a Maxwellian approximation for heat flow is less accurate than for plasma density or current. As temperature gradients become steeper, even extended XMHD models for Nernst advection will fail. Under these non-local conditions, when the electron mean free path is no longer small compared to the length scale of the temperature gradient, neither the heat flow nor the Nernst velocity are proportional to the local electron temperature gradient. While the effect of non-locality and magnetic fields upon the temperature profile has been explored before [17–19], non-local changes to the magnetic field have so far only been studied in kinetic simulations using Vlasov-Fokker-Planck (VFP) codes, which include the Nernst effect implicitly [20, 21]. Nernst advection therefore makes an excellent laboratory to measure kinetic effects, where changes to the heat dynamics directly affect the magnetic field.

We describe a laser-plasma experiment to measure the effect of heat flow on an applied magnetic field. Using laser-driven proton radiography [22] of an applied magnetic field, we demonstrate that Nernst advection dominates changes to the magnetic field in underdense plasmas on nanosecond timescales. Unlike previous experiments, we isolate Nernst advection and show that the magnetic field dynamics are decoupled from motion of the plasma.

We focused a 1.5 ns duration heater beam through a nitrogen gas target, propagating anti-parallel to the 3 T applied field as shown in Fig. 1. Laser intensities of  $84 \times 10^{16}$  Wcm<sup>-2</sup> were reached in a spot size of 19  $\mu$ m FWHM

85 over a Rayleigh length of  $\approx 1$  mm. This produced an  
 86 approximately cylindrically-symmetric plasma with elec-  
 87 tron densities of  $10^{18} - 10^{19} \text{ cm}^{-3}$  over a scale length of  
 88  $\sim 100 \mu\text{m}$ , with a temperature of around  $700 \pm 300 \text{ eV}$  at  
 89 the highest electron density, as estimated from the mea-  
 90 sured thermoelectric field (see Supplementary Material  
 91 for details). This gives a ratio between the cyclotron fre-  
 92 quency  $\omega_c$  and the collision frequency  $1/\tau_e$  described by  
 93 a Hall parameter around  $\omega_c \tau_e \approx 1 - 10$ . Under these  
 94 conditions, the magnetic field and heat flow are strongly  
 95 coupled, with the magnetic field restricting perpendicu-  
 96 lar heat flow, but heat flow also affecting the magnetic  
 97 field dynamics. The changes in the magnetic field are  
 98 described by [5]:

$$\frac{\partial \mathbf{B}}{\partial t} = \nabla \times (\mathbf{v}_B \times \mathbf{B}) + \nabla \times \left( \frac{1}{\mu_0 \sigma_{\perp}} \nabla \times \mathbf{B} \right) + \frac{\nabla T_e \times \nabla n_e}{en_e}, \quad (1)$$

99 where the first term describing advection is a combina-  
 100 tion of the hydrodynamic motion and the Nernst advec-  
 101 tion as  $\mathbf{v}_B = \mathbf{u} - (1 + \delta_{\perp}^c)(\mathbf{J}/en_e) + \mathbf{v}_N$ , where under our  
 102 magnetised conditions the Braginskii coefficient  $\delta_{\perp}^c \sim 0.1$ .  
 103 This gives  $\mathbf{v}_B \approx \mathbf{v}_e + \mathbf{v}_N$  [23], for electron motion  $\mathbf{v}_e$ .  
 104 We estimate a sound speed on the scale of  $10^5 \text{ m/s}$  and  
 105 a thermal diffusivity on the order of  $10^4 \text{ m}^2/\text{s}$ , giving a  
 106 thermal Péclet number of  $Pe \sim 10^{-2}$ . This makes heat  
 107 conduction dominant over convection, indicating the im-  
 108 portance of Nernst advection, while the Knudsen number  
 109  $\lambda_{\text{mfp},e}/l_T \approx 1$ , showing the importance of non-locality.  
 110 The Braginskii conductivity is around  $\sigma_{\perp} \sim 10^7 \text{ S/m}$ ,  
 111 giving a magnetic Reynolds number of  $Re_M \sim 100$  and  
 112 allowing us to neglect the magnetic diffusion and resis-  
 113 tivity gradient flow described by the second term. The  
 114 cylindrically-symmetric geometry is chosen such that the  
 115 final Biermann term for generating magnetic fields is neg-  
 116 ligible, with  $\nabla T_e \parallel \nabla n_e$ . Shots without an applied mag-  
 117 netic field showed no magnetic field generation. Under  
 118 our conditions the only possible contributions to changes  
 119 in the magnetic field are therefore Nernst advection and  
 120 hydrodynamic advection ('frozen-in-flow').

121 The hydrodynamic advection was studied using opti-  
 122 cal interferometry. The 1 ps-duration collimated probe  
 123 beam passed transversely through the plasma column,  
 124 with the interaction point re-imaged onto an Andor Neo  
 125 camera after passing through a Mach-Zehnder interfer-  
 126 ometer. The interferograms (examples shown in Fig. 2a.i)  
 127 measure a plasma column much longer than it is wide,  
 128 which was found to be largely symmetric by performing  
 129 separate Abel inversions of the top and bottom halves of  
 130 the data, before combining both halves to a symmetric  
 131 map. The resulting density map and radial density pro-  
 132 files are shown in Fig. 2a.ii-iii. The two laser shots were  
 133 conducted under the same conditions, with the probe  
 134 passing through the plasma at early and late times (0.4 ns  
 135 and 1.1 ns).

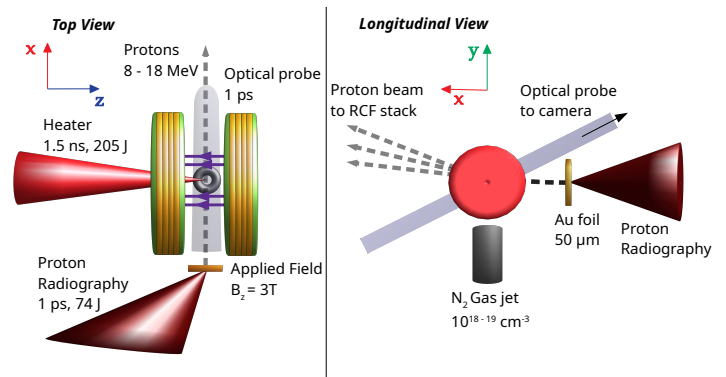


FIG. 1. Experimental layout shown from above (left) and from along the  $z$ -axis (right). The 1.5 ns-duration heater beam (solid red) is focussed along the  $z$ -axis to a point 2 mm above the gas jet nozzle. A 1 ps-duration proton radiography beam (solid red) is focussed onto a gold foil, producing a proton beam (grey dashed) which passes through the interaction point along the  $x$ -axis, perpendicular to the heater beam, and is deflected upwards by the applied magnetic field. The 1 ps-duration collimated optical probe beam (translucent grey) also passes through the interaction point in the  $x$ - $y$  plane, perpendicular to the heater beam.

136 The recovered density shown in the top panels of  
 137 Fig. 2a.ii-iii demonstrates that 0.4 ns after the start of  
 138 the heater beam, a plasma column has been formed with  
 139 a diameter of around  $300 \mu\text{m}$  over a length of slightly  
 140 under 2 mm longitudinally, with a peak density around  
 141  $10^{19} \text{ cm}^{-3}$ . At these relatively early times, the plasma  
 142 is not yet fully ionized and the plasma column shows no  
 143 sign of cavitation. As the heater beam continues to ion-  
 144 ize more gas and the plasma expands, however, a density  
 145 cavity forms inside the plasma column by 1.1 ns after the  
 146 start of the heater beam, shown in the bottom panels.

147 The magnetic field evolution was measured using proton  
 148 radiography performed using a broadband TNSA  
 149 proton source [22]. Protons were generated by focussing  
 150 a 1 ps duration laser pulse onto a  $50 \mu\text{m}$  thick gold foil  
 151 using an  $f/3$  off-axis paraboloid. This proton beam passed  
 152 from the foil, 20 mm from the interaction point, trans-  
 153 versely through the plasma column, before being mea-  
 154 sured by a stack of Gafchromic EBT3 radiochromic film  
 155 (RCF) 167 mm after the interaction point, giving a mag-  
 156 nification of 9.35. The proton intensity distribution mea-  
 157 sured by radiographs, as shown in Fig. 2b.i, can therefore  
 158 be used to reconstruct the magnetic fields through which  
 159 the protons have passed [24, 25]. Shots taken without the  
 160 applied magnetic field showed that the signal from elec-  
 161 tric fields was much weaker than the signal from magnetic  
 162 fields, with proton deflections below 0.1 mrad, around an  
 163 order of magnitude smaller than deflections when an ap-  
 164 plied field was present.

165 However, the proton beam in this experiment was def-  
 166 lected by both the signal region within the plasma and  
 167 also the constant applied magnetic field in a much larger  
 168 region surrounding the plasma. This blurs out the radi-  
 169 ographs and changes the symmetry of the signal. We

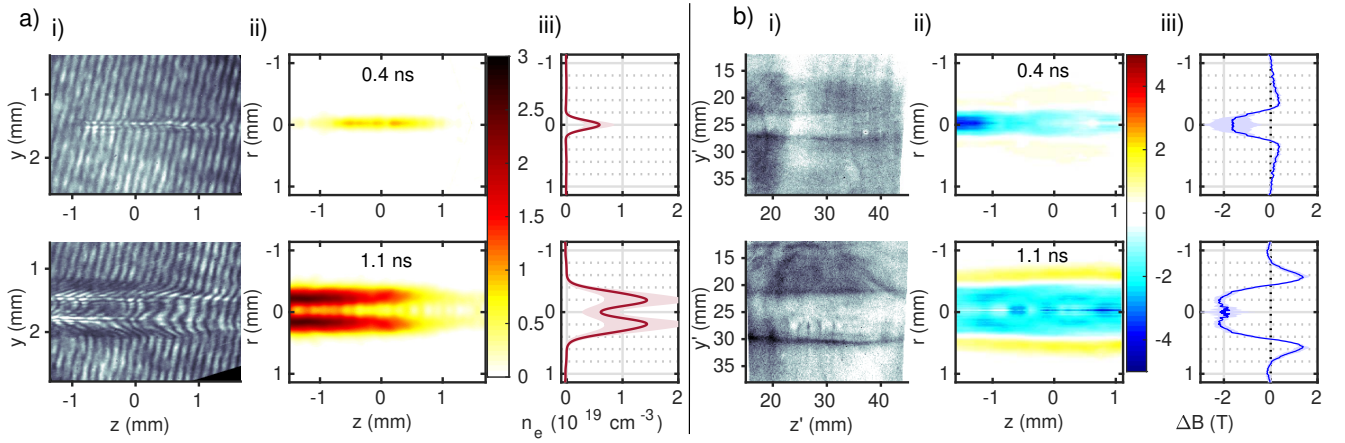


FIG. 2. a) Interferometry results measured 0.4 ns after the start of the heater beam (top panels) and 1.1 ns after (bottom). (i) The raw interferogram measured on the camera is shown on the left, with fringe shifts showing the presence of a long plasma column. (ii) From this interferogram we reconstruct a map of the plasma density, shown as a cross-section through the centre of the column. (iii) The longitudinally averaged mean of the radial plasma density profile is shown to the right of this, with the shaded region showing the standard deviation longitudinally. b) Radiography results measured at the same times. (i) The raw radiograph is shown on the left, with darker regions showing a higher proton dose. (ii) The change in the magnetic field reconstructed from the radiograph is shown as a cross-section through the centre of the plasma column, with (iii) the longitudinally averaged mean and standard deviation of the radial magnetic field profile to the right.

170 therefore used a deconvolution algorithm to remove the  
 171 effect of the background field, accounting for the finite  
 172 energy absorption range of the RCF, the broadband proton  
 173 source, and the deflection in the background field,  
 174 as described in ref. [26] (see Supplementary Material for  
 175 more details), with a spatial resolution of around  $50 \mu\text{m}$   
 176 for 10 MeV protons. The resulting monoenergetic radio-  
 177 graphs were largely antisymmetric, allowing us to recover  
 178 the magnetic fields separately from the thermoelectric  
 179 field. The recovered change in the magnetic fields is  
 180 shown in Fig. 2b.ii-iii, where on each of the two shots  
 181 the proton beam was timed such that the 10.6 MeV protons  
 182 most strongly absorbed in the third layer of the RCF  
 183 stack passed through the plasma simultaneously with the  
 184 optical probe to within the temporal resolution of 10s of  
 185 ps.

186 Shortly after the start of the heater beam, at 0.4 ns, a  
 187 strong reduction in the magnetic field strength by  $-2 \text{ T}$   
 188 in the central region is already visible in the top panel  
 189 of Fig. 2b.iii, despite no cavitation in the plasma den-  
 190 sity. The applied magnetic field is advected to the edge  
 191 of the plasma by heat flow, resulting in an increase in  
 192 the magnetic field strength further off-axis, at a radius  
 193 of around  $350 \mu\text{m}$ . The spatial size of the cavitation is  
 194 fairly uniform over a length of around 2 mm, with the  
 195 field cavitating over the whole of the hot plasma. This  
 196 decoupling of the magnetic field profile from the plasma  
 197 flow is a clear signature of the Nernst effect; this is the  
 198 first time this has been measured in experiment.

199 The magnetic field and density profiles at these two  
 200 different times are overlaid in Fig. 3a for comparison.  
 201 The magnetic field is advected to the sheath plasma re-  
 202 gion and within the hot plasma is reduced to less than a

203 third of its original strength. Fig. 3a shows that Nernst  
 204 advection is significantly faster than hydrodynamic mo-  
 205 tion under these conditions. Heat flow drives cavitation  
 206 in the magnetic field over a large region, before any cav-  
 207 itation occurs in the plasma density, with pre-heating  
 208 reaching out to  $r > 0.5 \text{ mm}$ . We can therefore estimate  
 209 the Nernst velocity at 0.4 ns by measuring the radius of  
 210 the peak magnetic field at different times, reconstructed  
 211 from five different proton radiographs taken on the same  
 212 shot (RCF layers 2-6, absorbing proton energies from  
 213  $7.6 - 18.3 \text{ MeV}$ ). This gives a measured Nernst veloc-  
 214 ity at these early times of  $(6 \pm 2) \times 10^5 \text{ m/s}$ .

215 The Nernst velocity gives an estimate for the heat flux  
 216 as  $\phi_q = 5n_e T_e v_N / 2$ , which can be compared to the free-  
 217 streaming heat flux  $\phi_{fs} = n_e T_e v_{th,e}$  for a thermal velocity  
 218  $v_{th,e}$ . Given that the electron thermal velocity at 700 eV  
 219 is  $1.6 \times 10^7 \text{ m/s}$ , we infer a heat flux at 0.4 ns at least one  
 220 tenth of the free-streaming limit, showing the importance  
 221 of correctly modelling the heat transport at these early  
 222 times. Indeed, the Braginskii estimate for the heat flow,  
 223 given the measured density and temperature profiles at  
 224 0.4 ns, reaches  $300 \text{ TW/m}^2$ . This corresponds to a pre-  
 225 dicted Nernst velocity of  $4 \times 10^5 \text{ m/s}$ , consistent with the  
 226 measured advection.

227 However, the Nernst velocity falls as time goes on and  
 228 the heat flow reduces, with the change in peak magnetic  
 229 field position between 0.4 ns and 1.1 ns corresponding to  
 230 an average advection velocity of just  $(2.7 \pm 1.0) \times 10^5 \text{ m/s}$ .  
 231 Measuring the half-width at half-maximum of the density  
 232 profile at 1.1 ns gives an average bulk velocity of  $\approx 3 \times$   
 233  $10^5 \text{ m/s}$ , which is comparable to the ion sound speed at  
 234 700 eV. Whereas at early times magnetic field advection  
 235 is dominated by hot electrons through the Nernst effect,

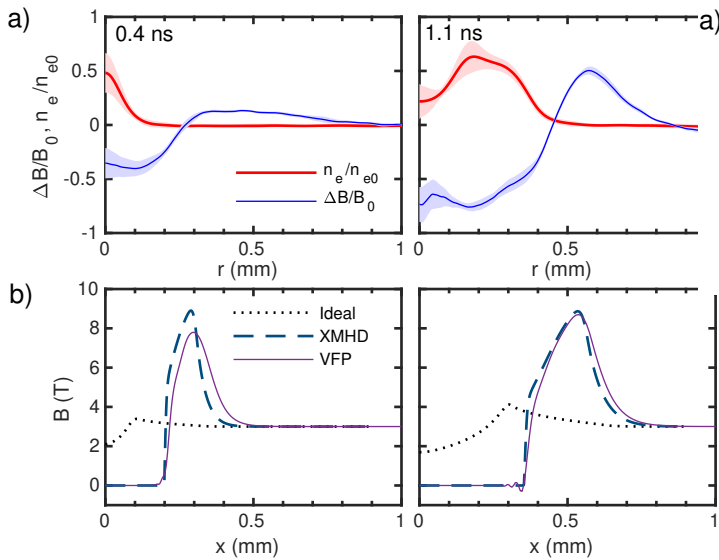


FIG. 3. (a) The reconstructed profiles of the magnetic field (blue) and density (red) against radius, measured at 0.4 ns (left panels) and 1.1 ns (right) and normalised to a background magnetic field  $B_0 = 3$  T and a fully-ionized density  $n_{e0} = 2.4 \times 10^{19} \text{ cm}^{-3}$ . Both profiles are longitudinally averaged over the central 1 mm of plasma, with the shaded area showing the standard deviation. (b) The magnetic field profile predicted from one-dimensional simulations, showing an ideal MHD model without the Nernst effect (dotted black line), an XMHD model including the thermoelectric Nernst term (dashed dark blue), and results from kinetic VFP simulations, with Nernst advection included implicitly (solid purple).

at later times hydrodynamic motion on the timescale of ion motion becomes more important.

We model the plasma and magnetic field evolution with CTC [27]— an XMHD code which includes Nernst advection with a flux-limited model of heat flow — and a kinetic VFP code, IMPACT [28], in a 1D planar geometry, to see the effects of the Nernst term and of different treatments of heat transport. Both simulations began with a uniform fully-ionized  $Z = 7$  plasma at a density of  $n_{e0} = 2.4 \times 10^{19} \text{ cm}^{-3}$  and modelled laser heating using a realistic temporal profile. Fig. 3b shows the predictions from IMPACT and the predictions from CTC both with and without the Nernst term. The scale of magnetic cavitation cannot be explained without invoking the Nernst effect, as ideal MHD simulations with the Nernst term turned off (shown by the black dotted line) predict only slight and slow-moving cavitation which approximately matches the density profile. Once the Nernst effect is included, however, the fluid and kinetic simulations (dashed and solid line respectively) closely agree and both capture the shape of the magnetic field profile at later times. The long tail in the magnetic field peak at 0.4 ns implies that the plasma was heated by additional processes beyond inverse bremsstrahlung over a much larger area than the initial laser spot, but as the plasma evolves the magnetic field profile shows the for-

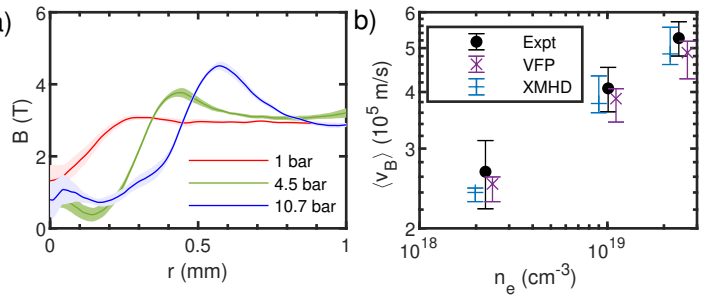


FIG. 4. a) The recovered magnetic field profiles measured 1.1 ns after the arrival of the heater beam for three different backing pressures, showing the mean and standard deviation of the magnetic field over a 1 mm long section in the middle of the gas jet. b) Comparing results from the simulations and the experiments, the average advection velocity of the magnetic field in the time up to 1.1 ns is measured by the position of the peak in the magnetic field.

mation of a steeper heat front.

That the fluid and kinetic simulations agree so closely is surprising, as both simulations predict mean free paths on the order of  $100 \mu\text{m}$ , where the fluid model should break down. In the one-dimensional simulations shown here, however, the increase in the magnetic field at the edge of the hot plasma means the Hall parameter at the heat front reaches  $\omega_c \tau_e \approx 10$  by 1.1 ns. In this regime the heat transport becomes limited by the electron gyroradius rather than by the mean free path, with the Nernst growth rate described by Sherlock and Bissell [29] changing from  $\tilde{N}\tau_{ei} \sim (\lambda_{\text{mfp},e}/l_T)^2 \approx 1$  to  $\tilde{N}\tau_{ei} \sim (r_c/l_T)^2 \lesssim 0.1$ . At early times the kinetic and fluid simulations predict different heat flows, but at later times the Nernst effect increasingly leads to a magnetic transport barrier which keeps the heat flow in a relatively local regime, even as the magnetic field inside the cavity falls to zero.

To further explore this effect, laser shots were taken at three different gas jet backing pressures. The resulting magnetic field profiles are shown in Fig. 4a, measured 1.1 ns after the start of the heater beam. At lower densities the plasma is less collisional, with a lower rate of inverse bremsstrahlung heating resulting in a colder plasma. The mean free path predicted by simulations increases to  $300 \mu\text{m}$  at 1 bar while the maximum Hall parameter increases to  $\omega_c \tau_e \approx 40$ . This means both that the speed of heat flow is lower at lower densities — leading to slower magnetic advection and less cavitation as observed in the experiment — and also that the magnetic barrier further constrains the heat flow. In a strongly magnetised plasma we would expect the rate of heat flow to scale as  $v_N \propto \tau_e^{-1} \propto n_e T_e^{-1.5}$  [23].

We estimate how the Nernst advection rates change with density by measuring the position of the peak in the magnetic field at 1.1 ns in both the experiment and 1D simulations without a flux-limiter; these results are shown in Fig. 4b. In all cases, the advection velocity

falls with decreasing density, with the simulations very closely reproducing the behaviour measured in experiment. Fitting the measured average advection velocities to a power law, however, gives a trend  $v_B \propto n_{e0}^{0.30 \pm 0.03}$ . Our simulations show that  $v_B \propto T_e^{0.2}$  in 1D and although the collision time is a factor of five higher at the lowest density, the advection velocity is only reduced by a factor of two. The stronger magnetisation localises the heat flow, but the Nernst advection is still faster than for a strongly magnetised plasma, particularly at early times before the magnetic barrier grows large.

In summary, we have made the first direct measurement of magnetic cavitation driven by heat flow rather than by bulk motion in the plasma. This magnetic cavitation is particularly relevant for experiments into magnetic reconnection – where rapid heating means that magnetic transport is often Nernst-dominated – and for inertial confinement fusion, where applied or self-generated magnetic fields have been shown to increase temperatures in the hot-spot and mitigate instability growth [18, 30, 31]. As described in refs. [6, 32], the expulsion of magnetic fields from the hottest regions of the plasma will increase the field strengths required for magnetised inertial confinement fusion techniques. We have shown that models without the Nernst term result in a spuriously high magnetic field within the plasma, and that under our moderately magnetized conditions XMHD models agree surprisingly well with kinetic simulations despite long mean free paths; the heat flow at the edge of the hot plasma remains relatively local due to the increase in the magnetic field outside the hot plasma.

The authors are grateful for the support of LLNL Academic Partnerships (B618488), EUROfusion Enabling Research Grants AWP17-ENR-IFE-CCFE-01 and AWP17-ENR-IFE-CEA-02, and UK EPSRC grants EP/P026796/1, EP/R029148/1, EP/M01102X/1 and EP/M011372/1. The authors particularly wish to thank the staff at Vulcan and Target Fabrication at the Central Laser Facility for all their support. Radiography calibration data from David Carroll and James Green were indispensable and we are grateful for IMPACT simulations conducted by Dominic Hill and advice with CTC from John Bissell. Part of this project was undertaken on the Viking Cluster, which is a high performance compute facility provided by the University of York. We are grateful for computational support from the University of York High Performance Computing service, Viking and the Research Computing team. The raw data and analysis code are available online at <https://doi.org/10.15124/bd949fdd-1c2c-4d04-b2eb-785065198a69>.

The experiment was designed by NW, CPR, and MPR and planned by CA, PB, GSH, OCE, LA, ZN, and NW. GSH and PB were the target area operators, and MN was the facility link scientist. CA led the proton radiography set-up, SA and GSH were responsible for the pulsed power magnet, OCE designed and built the optical probe layout, and KG built the system used for timing. PB, LA and MK worked on all aspects of the experiment. AD and CAW conducted fluid simulations, and AD, CA and CPR conducted VFP simulations with a code originally written by RJK. CA conducted the radiography and interferometry analysis with PB, and led the composition of the manuscript, with contributions and revisions from PB, GSH, OCE, RJK, ZN, CPR and NW.

\* Corresponding author

† Now at University of Bordeaux

‡ Now at First Light Fusion

§ Now at Shanghai Jiao Tong University

¶ Previously at Imperial College London

- [1] L. Biermann, *Zeitschrift Naturforschung Teil A* **5**, 65 (1950).
- [2] S. I. Braginskii, *Journal of Experimental and Theoretical Physics* **6**, 358 (1958).
- [3] M. G. Haines, *Plasma Phys. Control. Fusion* **28**, 1705 (1986).
- [4] A. B. Sefkow, S. A. Slutz, J. M. Koning, M. M. Marinak, K. J. Peterson, D. B. Sinars, and R. A. Vesey, *Physics of Plasmas* **21**, 072711 (2014).
- [5] J. R. Davies, R. Betti, P.-Y. Chang, and G. Fiksel, *Physics of Plasmas* **22**, 112703 (2015).
- [6] S. A. Slutz, M. C. Herrmann, R. A. Vesey, A. B. Sefkow, D. B. Sinars, D. C. Rovang, K. J. Peterson, and M. E. Cuneo, *Physics of Plasmas* **17**, 056303 (2010).
- [7] M. Hohenberger, P.-Y. Chang, G. Fiksel, J. P. Knauer, R. Betti, F. J. Marshall, D. D. Meyerhofer, F. H. Séguin, and R. D. Petrasso, *Physics of Plasmas* **19**, 056306 (2012).
- [8] L. J. Perkins, D. D.-M. Ho, B. G. Logan, G. B. Zimmerman, M. A. Rhodes, D. J. Strozzi, D. T. Blackfield, and S. A. Hawkins, *Physics of Plasmas* **24**, 062708 (2017).
- [9] J. D. Moody, B. B. Pollock, H. Sio, D. J. Strozzi, D. D.-M. Ho, C. A. Walsh, G. E. Kemp, B. Lahmann, S. O. Kucheyev, B. Koziolowski, E. G. Carroll, J. Kroll, D. K. Yanagisawa, J. Angus, B. Bachmann, S. D. Bhandarkar, J. D. Bude, L. Divol, B. Ferguson, J. Fry, L. Hagler, E. Hartouni, M. C. Herrmann, W. Hsing, D. M. Holunga, N. Izumi, J. Javedani, A. Johnson, S. Khan, D. Kalantar, T. Kohut, B. G. Logan, N. Masters, A. Nikroo, N. Orsi, K. Piston, C. Provencher, A. Rowe, J. Sater, K. Skulina, W. A. Stygar, V. Tang, S. E. Winters, G. Zimmerman, P. Adrian, J. P. Chittenden, B. Appelbe, A. Boxall, A. Crilly, S. O'Neill, J. Davies, J. Peebles, and S. Fujioka, *Phys. Rev. Lett.* **129**, 195002 (2022).
- [10] K. Behnia and H. Aubin, *Rep. Prog. Phys.* **79**, 046502 (2016).
- [11] A. Nishiguchi, T. Yabe, M. G. Haines, M. Psimopoulos, and H. Takewaki, *Phys. Rev. Lett.* **53**, 262 (1984).
- [12] L. Willingale, A. G. R. Thomas, P. M. Nilson, M. C. Kaluza, S. Bandyopadhyay, A. E. Dangor, R. G. Evans, P. Fernandes, M. G. Haines, C. Kamperidis, R. J. Kingham, S. Minardi, M. Notley, C. P. Ridgers, W. Rozmus, M. Sherlock, M. Tatarakis, M. S. Wei, Z. Najmudin, and K. Krushelnick, *Phys. Rev. Lett.* **105**, 095001 (2010).
- [13] C. Li, F. Séguin, J. Frenje, N. Sinenian, M. Rosenberg, M.-E. Manuel, H. Rinderknecht, A. Zylstra, R. Petrasso, P. Amendt, O. Landen, A. Mackinnon, R. Town, S. Wilks, R. Betti, D. Meyerhofer, J. Soures, J. Hund, J. Kilkenny, and A. Nikroo, *Nucl. Fusion* **53**, 073022 (2013).
- [14] L. Lancia, B. Albertazzi, C. Boniface, A. Grisollet, R. Riquier, F. Chaland, K.-C. Le Thanh, P. Mellor, P. Antici, S. Buffechoux, S. N. Chen, D. Doria, M. Nakatsutsumi, C. Peth, M. Swantusch, M. Stardubtsev, L. Palumbo, M. Borghesi, O. Willi, H. Pépin, and J. Fuchs, *Phys. Rev. Lett.* **113**, 235001 (2014).

- [15] L. Gao, P. M. Nilson, I. V. Igumenshchev, M. G. Haines, D. H. Froula, R. Betti, and D. D. Meyerhofer, *Phys. Rev. Lett.* **114**, 215003 (2015).
- [16] E. R. Tubman, A. S. Joglekar, A. F. A. Bott, M. Borghesi, B. Coleman, G. Cooper, C. N. Danson, P. Durey, J. M. Foster, P. Graham, G. Gregori, E. T. Gumbrell, M. P. Hill, T. Hodge, S. Kar, R. J. Kingham, M. Read, C. P. Ridgers, J. Skidmore, C. Spindloe, A. G. R. Thomas, P. Treadwell, S. Wilson, L. Willingale, and N. C. Woolsey, *Nat. Commun.* **12**, 334 (2021).
- [17] G. Gregori, S. H. Glenzer, J. Knight, C. Niemann, D. Price, D. H. Froula, M. J. Edwards, R. P. J. Town, A. Brantov, W. Rozmus, and V. Y. Bychenkov, *Phys. Rev. Lett.* **92**, 205006 (2004).
- [18] D. H. Froula, J. S. Ross, B. B. Pollock, P. Davis, A. N. James, L. Divol, M. J. Edwards, A. A. Offenberger, D. Price, R. P. J. Town, G. R. Tynan, and S. H. Glenzer, *Phys. Rev. Lett.* **98**, 135001 (2007).
- [19] R. J. Henchen, M. Sherlock, W. Rozmus, J. Katz, D. Cao, J. P. Palastro, and D. H. Froula, *Phys. Rev. Lett.* **121**, 125001 (2018).
- [20] C. P. Ridgers, R. J. Kingham, and A. G. R. Thomas, *Phys. Rev. Lett.* **100**, 075003 (2008).
- [21] A. S. Joglekar, C. P. Ridgers, R. J. Kingham, and A. G. R. Thomas, *Phys. Rev. E* **93**, 043206 (2016).
- [22] M. Borghesi, J. Fuchs, S. V. Bulanov, A. J. MacKinnon, P. K. Patel, and M. Roth, *Fusion Science and Technology* **49**, 412 (2006).
- [23] C. A. Walsh, J. P. Chittenden, D. W. Hill, and C. Ridgers, *Physics of Plasmas* **27**, 022103 (2020).
- [24] N. L. Kugland, D. D. Ryutov, C. Plechaty, J. S. Ross, and H.-S. Park, *Review of Scientific Instruments* **83**, 101301 (2012).
- [25] M. F. Kasim, A. F. A. Bott, P. Tzeferacos, D. Q. Lamb, G. Gregori, and S. M. Vinko, *Phys. Rev. E* **100**, 033208 (2019).
- [26] C. Arran, C. P. Ridgers, and N. C. Woolsey, *Matter and Radiation at Extremes* **6**, 046904 (2021), <https://doi.org/10.1063/5.0054172>.
- [27] J. J. Bissell, C. P. Ridgers, and R. J. Kingham, *Phys. Rev. Lett.* **105**, 175001 (2010).
- [28] R. J. Kingham and A. R. Bell, *Journal of Computational Physics* **194**, 1 (2004).
- [29] M. Sherlock and J. J. Bissell, *Phys. Rev. Lett.* **124**, 055001 (2020).
- [30] P. Y. Chang, G. Fiksel, M. Hohenberger, J. P. Knauer, R. Betti, F. J. Marshall, D. D. Meyerhofer, F. H. Séguin, and R. D. Petrasso, *Phys. Rev. Lett.* **107**, 035006 (2011).
- [31] C. A. Walsh, K. McGlinchey, J. K. Tong, B. D. Appelbe, A. Crilly, M. F. Zhang, and J. P. Chittenden, *Physics of Plasmas* **26**, 022701 (2019).
- [32] R. D. McBride and S. A. Slutz, *Physics of Plasmas* **22**, 052708 (2015).
- [33] See Supplemental Material at [url] for additional details of the experimental set-up, analysis, and simulations, which includes Refs. [34-41].
- [34] R. A. Snavely, M. H. Key, S. P. Hatchett, T. E. Cowan, M. Roth, T. W. Phillips, M. A. Stoyer, E. A. Henry, T. C. Sangster, M. S. Singh, S. C. Wilks, A. MacKinnon, A. Offenberger, D. M. Pennington, K. Yasuike, A. B. Langdon, B. F. Lasinski, J. Johnson, M. D. Perry, and E. M. Campbell, Intense High-Energy Proton Beams from Petawatt-Laser Irradiation of Solids, *Phys. Rev. Lett.* **85**, 2945 (2000).
- [35] S. C. Wilks, A. B. Langdon, T. E. Cowan, M. Roth, M. Singh, S. Hatchett, M. H. Key, D. Pennington, A. MacKinnon, and R. A. Snavely, Energetic proton generation in ultra-intense laser–solid interactions, *Physics of Plasmas* **8**, 542 (2001).
- [36] W. H. Richardson, Bayesian-Based Iterative Method of Image Restoration, *J. Opt. Soc. Am.*, *JOSA* **62**, 55 (1972).
- [37] L. B. Lucy, An iterative technique for the rectification of observed distributions, *The Astronomical Journal* **79**, 745 (1974).
- [38] D. D. Hickstein, S. T. Gibson, R. Yurchak, D. D. Das, and M. Ryazanov, A direct comparison of high-speed methods for the numerical Abel transform, *Review of Scientific Instruments* **90**, 065115 (2019).
- [39] E. W. Hansen and P.-L. Law, Recursive methods for computing the Abel transform and its inverse, *J. Opt. Soc. Am. A*, *JOSAA* **2**, 510 (1985).
- [40] E. Hansen, Fast Hankel transform algorithm, *IEEE Trans. Acoust. Speech Signal Process.* **33**, 666 (1985).
- [41] M. Takeda, H. Ina, and S. Kobayashi, Fourier-transform method of fringe-pattern analysis for computer-based topography and interferometry, *J Opt Soc Am* **72**, 156 (1982).